

RESAR-BEV: An Explainable Progressive Residual Autoregressive Approach for Camera-Radar Fusion in BEV Segmentation

Zhiwen Zeng, Yunfei Yin*, Member, IEEE, Zheng Yuan, Argho Dey, and Xianjian Bao

Abstract—Bird’s-Eye-View (BEV) semantic segmentation provides comprehensive environmental perception for autonomous driving but suffers multi-modal misalignment and sensor noise. We propose RESAR-BEV, a progressive refinement framework that advances beyond single-step end-to-end approaches: (1) progressive refinement through residual autoregressive learning that decomposes BEV segmentation into interpretable coarse-to-fine stages via our Drive-Transformer and Modifier-Transformer residual prediction cascaded architecture, (2) robust BEV representation combining ground-proximity voxels with adaptive height offsets and dual-path voxel feature encoding (max+attention pooling) for efficient feature extraction, and (3) decoupled supervision with offline Ground Truth decomposition and online joint optimization to prevent overfitting while ensuring structural coherence. Experiments on nuScenes demonstrate RESAR-BEV achieves state-of-the-art performance with 54.0% mIoU across 7 essential driving-scene categories while maintaining real-time capability at 14.6 FPS. The framework exhibits robustness in challenging scenarios of long-range perception and adverse weather conditions.

Index Terms—Autonomous Driving, Bird’s-Eye-View (BEV) Segmentation, Camera-Radar Fusion, Residual Autoregressive Learning, Interpretability.

I. INTRODUCTION

AUTONOMOUS driving systems require comprehensive 3D environment understanding to ensure safe navigation. While conventional perception tasks (e.g., object detection, semantic segmentation) operate within camera frustum views, Bird’s Eye View (BEV) representation has emerged as a pivotal paradigm for unifying multi-sensor inputs (including cameras, radars, and LiDARs) into a cohesive 3D scene representation.

BEV segmentation partitions BEV space into semantic regions like drivable areas and vehicles. Current approaches predominantly follow two paradigms: geometry-based methods (e.g., IPM [1]) requiring precise calibration but lacking robustness, and learning-based methods (e.g., BEVFormer [2], Bev-locator [3]) automatically learning cross-modal correlations but needing careful design to address noise and misalignment. Both methodologies share an end-to-end single-step mapping from sensor inputs to BEV space (Fig.1 (a)), inevitably leading to irreversible errors in challenging scenarios like occluded regions and long-range perception, primarily due to: imperfect

This work was submitted to IEEE Transactions on Intelligent Transportation Systems (T-ITS) on 09-May-2025

* Corresponding author.

Zhiwen Zeng, Yunfei Yin, Zheng Yuan, and Argho Dey are with the College of Computer Science, Chongqing University, Chongqing 400044, China (e-mail: zzwzengi@Outlook.com; yinyunfei@cqu.edu.cn; yuanzheng@cqu.edu.cn; arghomridul05@gmail.com).

Xianjian Bao is with the Department of Computer Science, Maharishi University of Management, Fairfield, IOWA, USA (e-mail: xibao@mum.edu).

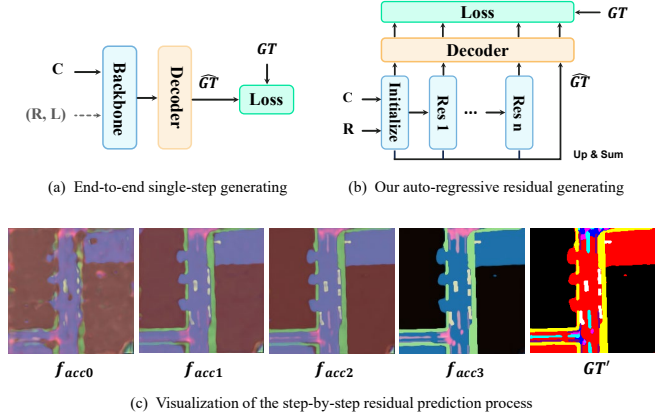


Fig. 1. (a) Previous single-step end-to-end multimodal BEV scene segmentation approach; (b) Our proposed progressive autoregressive residual prediction method with multi-resolution Ground Truth and multi-stage loss supervision; (c) Visualization of the RAF module’s multi-scale feature generation and accumulation process through decoder mapping to BEV semantics, followed by upsampling to uniform resolution.

depth estimation in geometry-based methods or global attention mechanisms deviation in learning-based approaches, combined with an inherent “all-or-nothing” prediction paradigm that forces networks to generate final BEV layouts in one pass while disregarding the intrinsic ambiguity of 2D-to-3D transformation. While recent works adopt multimodal fusion and temporal smoothing [4]–[8], they treat BEV segmentation atomically, neglecting hierarchical spatial reasoning from road topology to lane details.

Inspired by residual learning and autoregressive methodologies, we presents RESAR-BEV, reformulating BEV segmentation through progressive residual refinement. Our key insight posits that BEV space construction should be achieved through iterative local refinement rather than global one-shot prediction. As illustrated in Fig.1 (b), RESAR-BEV decomposes the task into: (1) coarse initialization generating low-resolution BEV estimation; (2) residual cascade refinement where compact subnetworks progressively predict and accumulate residuals; (3) hierarchical supervision applies stage-specific losses - enforcing topological consistency in early stages and pixel-level precision in later stages, with final segmentation loss on the accumulated output. Evaluated on the nuScenes dataset, our framework demonstrates the anticipated progressive residual prediction behavior (Fig.1 (c)). The residual mechanism effectively isolates errors to specific refinement stages, enabling interpretable generating process - achieving rapid convergence in simple scenarios while triggering deeper optimization for complex regions. Our main contributions are

as follows:

- 1) Progressive Residual Autoregressive Learning: We decompose BEV segmentation into an iterative process of "coarse estimation \rightarrow residual refinement \rightarrow hierarchical supervision." With a shared-private cascaded Transformer, multi-scale GT decomposition, and dynamic gating, it stabilizes training, surpassing single-step end-to-end and localizing errors to specific stages.
- 2) Ground-Aware BEV Optimization: We introduce ground-proximity voxels with adaptive height offsets, enhancing BEV spatial modeling through our improved dual-path radar encoding (max+attention pooling) with intermediate feature fusion to boost long-range and low-light robustness at minimal computational overhead.
- 3) Decoupling Supervision and Prediction: We employ offline pre-training of a GT decomposition network and online joint optimization of residual and segmentation losses to mitigate overfitting. Early stages capture global structures while later stages refine local details, emulating human driving cognition, with inherent support for visual interpretability analysis.

II. RELATED WORK

BEV representation is fundamental for 3D object detection [9], [10] and HD map segmentation [11], [12], yet challenges persist in cross-modal alignment, progressive refinement, and model interpretability. In this section, we analyze these gaps through three key dimensions.

A. BEV Segmentation Paradigms

Early BEV segmentation adopted implicit geometric modeling, learning image-to-BEV mappings directly through neural networks (VED [13] with VAEs, VPN [14] with MLPs). However, their purely data-driven nature without geometric priors constrained performance in complex scenarios.

Explicit geometric modeling has become mainstream by incorporating geometric priors for improved robustness. Early approaches primarily used Inverse Perspective Mapping (IPM [1]), which transforms camera views to BEV via geometric projection. While relying on idealized assumptions (e.g., flat ground, precise calibration), IPM established key geometric constraints that guided subsequent research.

The Lifting & Unlifting paradigm significantly advanced explicit 3D modeling for view transformation. Lifting methods (Image \rightarrow 3D \rightarrow BEV) first project image features into 3D space before BEV mapping. LSS [15] pioneered this approach through soft depth distribution estimation, while BEVDet [16] optimized feature extraction and FIERY [17] enhanced dynamic understanding via temporal fusion. BEV-Car [11] employed direct voxel projection, preserving features at higher computational cost. Conversely, Unlifting methods (BEV Query \rightarrow Image) use BEV queries for reverse projection. DETR3D [18] introduced Transformer-based queries, improved by Deformable DETR's [19] learnable sampling. BEVFormer [2] enhanced cross-view attention with temporal fusion, and BEVSegFormer [20] adapted queries specifically

for segmentation tasks. These approaches balanced accuracy and efficiency in feature transformation.

The paradigm has shifted from purely data-driven implicit methods to geometry-aware hybrid approaches, optimizing the accuracy-efficiency-interpretability trade-off in BEV perception. Following this latest paradigm, our work leverages "unlifting" to enable interactions between BEV queries and multi-scale image features.

B. Multi-Model Fusion for BEV Perception

Multimodal fusion has become crucial for robust BEV segmentation, overcoming single-sensor (e.g., camera) limitations in challenging conditions (e.g., night, rain) through two main approaches: camera-LiDAR and camera-radar fusion.

In camera-LiDAR fusion, BEVFusion [21] employs feature concatenation for efficient fusion, while TransFusion [22] leverages Transformer for finer cross-modal feature interaction. For cost-effective radar sensors, researchers have proposed innovative approaches: Simple-BEV [23] achieves rapid fusion via grid-based processing, FISHING [24] introduces category-first pooling, CRN [25] incorporates deformable attention mechanisms, and BEVGuide [26] proposes a unified BEV space query method. These advancements collectively drive the evolution of fusion strategies from early-stage simple feature concatenation to attention-based adaptive fusion.

Recent works have introduced more innovative approaches. BEVFormer v2 [27] introduces memory mechanisms to store historical BEV features; StreamPETR [28] enhances dynamic video stream detection by propagating object queries across time; RecurrentBEV [29] proposes a long-sequence fusion framework for object detection; and DualBEV [30] introduces a unified 3D-to-2D feature transformation approach. Bevtsr [31] presents a BEV-text retrieval system using LLM-processed descriptions and knowledge graph embeddings. Our method implements early dual-branch feature extraction: an vision extraction network and optimized voxel feature encoder, followed by intermediate cross-modal feature fusion.

C. Autoregressive Residual Learning and Interpretability

While progressive residual learning has demonstrated success in image segmentation (e.g., RMS-UNet [32]) and autoregressive image generation (e.g., VAR [33], RQ-VAE [34]), its potential in BEV perception remains largely unexplored. Current BEV segmentation methods predominantly adopt a single-step end-to-end global prediction paradigm (e.g., CVT [35], SparseFusion3D [36]), which lacks explicit supervision during the generation process. This monolithic approach suffers from irreversible error accumulation and behavioral misalignment with human driving cognition, which progressively refines scene understanding from coarse road topology to fine lane boundaries—a process fundamentally mismatched with parallel, single-step decoding paradigms. Inspired by this observation, our model decomposes the task of constructing the entire BEV segmentation map into relatively independent residuals and achieves a coarse-to-fine generation process through an autoregressive mechanism.

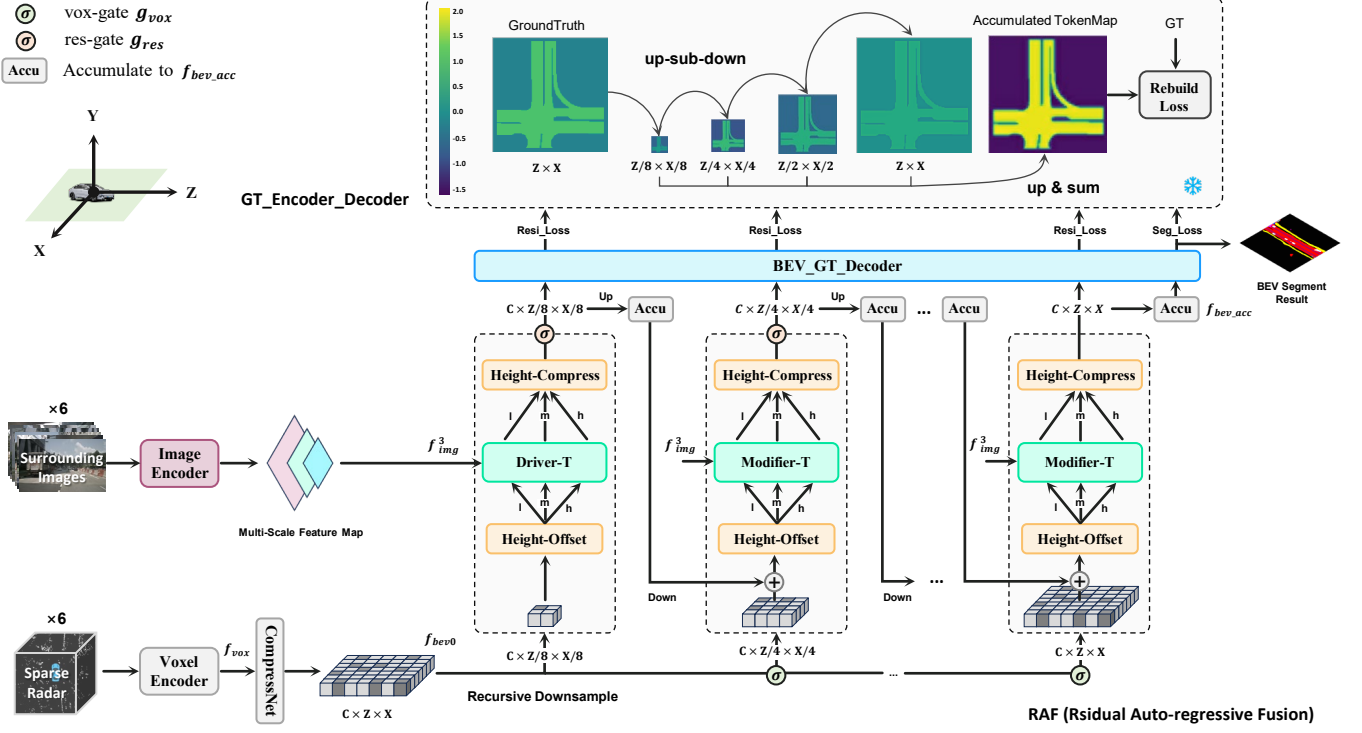


Fig. 2. Our Progressive Residual-Autoregressive BEV Segmentation Framework: (a) GT-Encoder-Decoder decomposes GroundTruth into multi-resolution residuals for hierarchical supervision; (b) Dual-branch encoder processes camera and radar inputs. The RAF module’s Driver-T generates low-resolution BEV via cross-modal attention (with dynamic Height-Offset/Compress for ground features), followed by Modifier-T predicting multi-scale residuals through autoregressive refinement (integrating historical outputs and radar features via resolution/channel-wise gates); (c) Each stage computes residual difference losses via BEV-GT-Decoder, with the final output generating segmentation maps and segmentation loss.

III. METHOD

A. Multi-Scale Ground-Truth Token Maps Decomposition

Unlike previous approaches that directly predict full-resolution binary segmentation maps from sensor inputs, we propose a hierarchical residual representation learning paradigm based on inverse decomposition of Ground Truth (GT). As illustrated in Fig. 2, given annotation GT with dimensions $C \times Z \times X$ where C denotes the number of classes, our method progressively decomposes GT into multi-scale token maps (TP_s). Each TP encodes distinct hierarchical semantic information: global structure for lower-resolution TP_s , while detailed boundary for higher-resolution TP_s .

GT Decomposition: Inspired by the multi-scale residual discretization in RQ-VAE [34], we design an up-sub-down decomposition process (Alg. 1) that progressively decomposes the original GT ($Z \times X$) into multi-scale token maps TP_i . The process initializes the GT as residual R_1 , then at each level i , downsampling R_i to TP_i with resolution $Z/2^{N-i} \times X/2^{N-i}$ while updating R_{i+1} through residual subtraction, until finally outputting the last residual R_N as full-resolution TP_N . To ensure numerical stability and suppress noise propagation in decomposition, we propose a cascaded residual update mechanism combining dynamic gating $\sigma(\theta)$ and $\tanh()$ nonlinearity:

$$R_{i+1} = R_i - \sigma(\theta) \odot \tanh(\text{Down}(R_i)) \quad (1)$$

where the $\tanh()$ activation (Lipschitz constant $L = 1$) confines each token map TP_i within $(-1, 1)$, enabling sta-

ble residual fluctuations around binary ground truth values while preventing feature explosion that could impair BEV-GT-Decoder convergence. The resolution- and channel-wise gating $(\sigma(\theta) \in (0, 1)^{(N \times C)})$ adaptively modulates cross-scale residual retention, maintaining balanced feature transitions across BEV hierarchies through learnable per-channel attenuation. In the downsampling process, we introduce a hybrid operator combining average pooling with learnable channel-separated convolutions, enabling the model to preserve local geometric structures while dynamically adjusting cross-resolution feature distributions. During upsampling, for geometric consistency, parameter-free bicubic interpolation maintains exact alignment between upsampled TP_i and reconstructed \hat{GT} , where $\hat{GT} = \sum_i U(TP_i)$ is optimized via Residual Dice Loss (Eq. 6) to match BEV segmentation targets.

The pretrained GT-Encoder-Decoder provides fixed multi-scale supervision for the autoregressive BEV network. Offline decomposition during annotation maintains real-time inference without computational overhead.

B. Multi-Modal Data Encoding

Our model employs two complementary modalities as input: (1) visual cameras that are semantically rich but lack depth information, and (2) radar point clouds that provide precise spatial localization but are highly sparse. Before feature fusion, they are processed by independent encoding networks.

Algorithm 1 Multi-scale Ground Truth Decomposition

Input: Original mask $GT \in \mathbb{R}^{C \times Z \times X}$, levels N
Output: Token maps $\{TP_i\}_{i=1}^N$, reconstructed \hat{GT}

- 1: DECOMPOSE(GT, N)
- 2: $R_1 \leftarrow GT$
- 3: $\hat{GT} \leftarrow 0$
- 4: **for** $i = 1$ to $N - 1$ **do**
- 5: $TP_i \leftarrow \tanh(\text{AVGPOOLCONV}(R_i, (\frac{Z}{2^{N-i}}, \frac{X}{2^{N-i}})))$
- 6: $\hat{TP}_i \leftarrow \text{BICUBIC}(TP_i, (Z, X))$
- 7: $R_{i+1} \leftarrow R_i - \sigma(\theta_i^{(C)}) \odot \hat{TP}_i$
- 8: $\hat{GT} \leftarrow \hat{GT} + \hat{TP}_i$
- 9: **end for**
- 10: $TP_N \leftarrow \tanh(R_N)$
- 11: $\hat{GT} \leftarrow \hat{GT} + TP_N$
- 12: **return** $\{TP_i\}_{i=1}^N, \hat{GT}$

Images Encoding: The image encoder is built upon the ResNet-101 [37] architecture, which effectively mitigates the vanishing gradient problem in deep networks through residual connections. Specifically, 6 synchronized images ($H \times W$) are fed into the first three feature sub-layers, generating multi-scale feature maps. To standardize the channel dimensions, each sub-layer output is followed by a channel compression convolution (1×1). The final outputs consist of three feature maps with spatial resolutions of $1/4, 1/8$, and $1/16$ of the original image size, denoted as f_{img}^3 .

Radar Encoding: We employ a voxel-based point cloud feature encoding method to achieve BEV-aligned representation. To mitigate radar sparsity, we aggregate and align point clouds from 6 consecutive timestamps. A 3D voxel grid $\mathcal{V} \in \mathbb{R}^{Z \times Y \times X}$ is initialized in the front-view camera coordinate system, where raw point clouds are discretized into voxel cells. Each cell is normalized to 10 points via random dropout or zero-padding. Based on the VFE [38], we propose a dual-path pooling enhancement: Each 6-dim point feature (x, y, z, vx, vy, rcs) is first projected into a D-dim space. Then, max-pooling extracts salient local features p_{max} , while attention-pooling (weighted aggregation of point cloud features through attention mechanisms) computes contextual features p_{attn} . As shown in Fig. 3, point-wise features are concatenated with both pooled features $[p; p_{max}; p_{attn}] \in \mathbb{R}^{3D}$ and compressed back to D-dim via an MLP network. This encoding process is cascaded in two stages, followed by voxel-wise max-pooling to generate the final compact representation $f_{vox} \in \mathbb{R}^{D \times Z \times Y \times X}$.

C. Ground-Proximity Lifting and Unlifting Process

In 3D-to-2D perspective interaction, the mapping between the imaging plane and voxel grid is established through camera intrinsics: each pixel's ray penetrates the grid, which samples features from corresponding pixels. The key (unlifting) lies in computing grid coordinates for each pixel, enabling BEV sampling. Previous methods [11], [23] use dense ego-centric

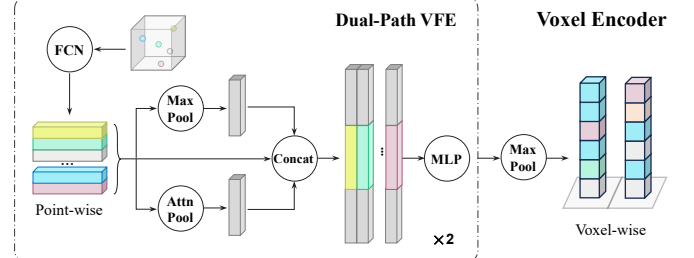
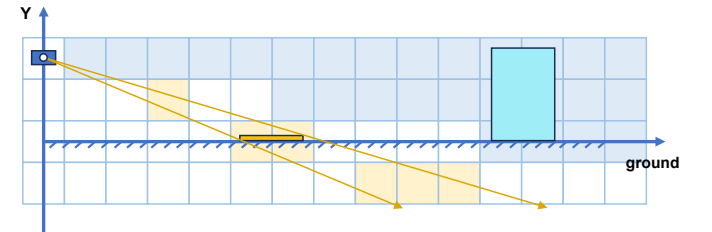


Fig. 3. Voxel feature extraction: we normalize each voxel to 10 points, then extract $C \times 10$ features via point-wise encoding. Apply parallel max/attention-pooling, concatenate with original features ($3C \times 10$), and compress to C channels via MLP. Repeat twice, then max-pool for final voxel features.

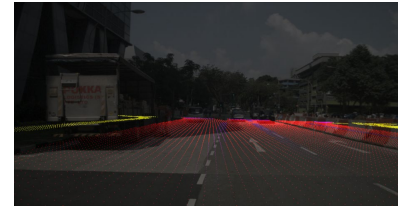
voxel grids but face two drawbacks: high computational cost and irrelevant background noise (e.g., sky, buildings). Fig. 4(a) shows grid regions above the camera are invalid, with projection errors increasing with distance to ground. Backprojection (Fig. 4(b)) reveals only the lower half of the image meaningfully interacts with grid attention.

Based on these observations, we propose ground-proximity: BEV modeling should focus only on grid features near the ground. However, due to camera height uncertainty, the ground plane's position is ambiguous in camera-centric coordinates. To address this, we introduce a height prior $Y_{gr}^{(i)}$ for each camera and learnable offset rate $Y_{drift}^{(i)} \in [0, 1]$, enabling dynamic adaptation to varying ground elevations:

$$Y_{new}^{(i)} = Y_{gr}^{(i)} + offset_{min} + Y_{drift}^{(i)} \cdot (offset_{max} - offset_{min}) \quad (2)$$



(a) **Lifting:** Pixel-to-grid ray interaction between the camera frustum plane and 3D space



(b) **Unlifting:** BEV grid back-projection onto the image plane

Fig. 4. Lifting and Unlifting Visualization Based on Camera Sensor Intrinsic.

D. Residual Auto-regressive Fusion

We propose a progressive Residual Auto-regressive Fusion (RAF) module, which consists of a BEV-initializing Drive stage and a multiscale residual-optimizing Modify stage. Each stage includes: (i) height-aware positional offsets, (ii) cross-attention Transformer decoders (Driver-T/Modifier-T),

and (iii) height compressors. RAF: (1) integrates hierarchical voxel features, (2) applies iterative vision-radar cross-modal attention, and (3) refines features via residual accumulation. The output is projected to BEV space by a BEV-GT-Decoder for high-precision segmentation.

Drive Stage: In this initial stage, a low-resolution token map generates a coarse-grained representation of the high-resolution *GT*. Specifically, the dense voxel feature f_{vox} is compressed along the Y-axis and channels via CompressNet yielding a 2D BEV feature $f_{bev_init} \in \mathbb{R}^{(D, Z, X)}$. A convolutional network then downsamples it by 1/8 to produce $f_{bev0} \in \mathbb{R}^{(D, Z/8, X/8)}$ as input of the first-level module. Here, a Height-Offset module enriches f_{bev0} with low-, mid-, and high-level height information, followed by the Driver-T interacting with multi-scale image features $f_{img}^{(3)}$ (Fig. 5). This module employs deformable attention [39] to efficiently model BEV-space locality via dynamic sampling - where f_{bev0} is back-projected onto the image plane for multi-head, multi-scale feature sampling - reducing computation while precisely attending to critical regions. Each grid attends to \mathcal{P} reference points with learnable offsets near the projected locations and fuses features adaptively. The Height-Compress module then fuses height-varying features into the lowest-resolution feature f'_{bev0} . In the RAF, f'_{bev0} is upsampled to the final resolution (D, Z, X) using Bicubic interpolation (consistent with Alg. 1) and accumulated into the zero-initialized f_{bev_acc} . Meanwhile, a learnable convolution downsample f_{bev_acc} to $(D, Z/4, X/4)$, generating f_{bev1} for the following residual prediction iteration.

Modify Stage: This stage employs a three-level autoregressive refinement process while preserving identical behavior to *GT* decomposition process. As detailed in Alg. 1, in the TP_s ' generation phase, the *GT* is decomposed hierarchically through a gated mechanism formulated as:

$$GT = \sigma(\theta_0) \cdot TP_0 + \sigma(\theta_1) \cdot TP_1 + \sigma(\theta_2) \cdot TP_2 + TP_3 \quad (3)$$

where all TP_s are processed by $\tanh()$ activation for value compression. Viewed right-to-left, this represents the BEV segmentation map generation process. Notably, all but the final residual term (which maintains minimal magnitude) are modulated by Sigmoid gates $\sigma(\theta_i)$. To ensure behavioral consistency with *GT* decomposition, we introduce resolution- and channel-wise learnable residual gating parameters g_{res} at each autoregressive stage (except the final level), dynamically controlling the influence of current TP_i on the accumulated BEV feature f_{bev_acc} . Each level's input features aggregate previous residual outputs:

$$f_{bevi} = \text{Down} \left(\sum_{k=1}^{i-1} \text{Up}(g_{resk} \cdot f'_{bevk}) \right) \quad (4)$$

where $\text{Up}(\cdot)$ /Down(\cdot) denote feature resampling. Voxel features obtained via multi-scale downsampling are fused with f_{bevi} as input for spatial enhancement. To mitigate conflicts between voxel features and residual accumulations that may

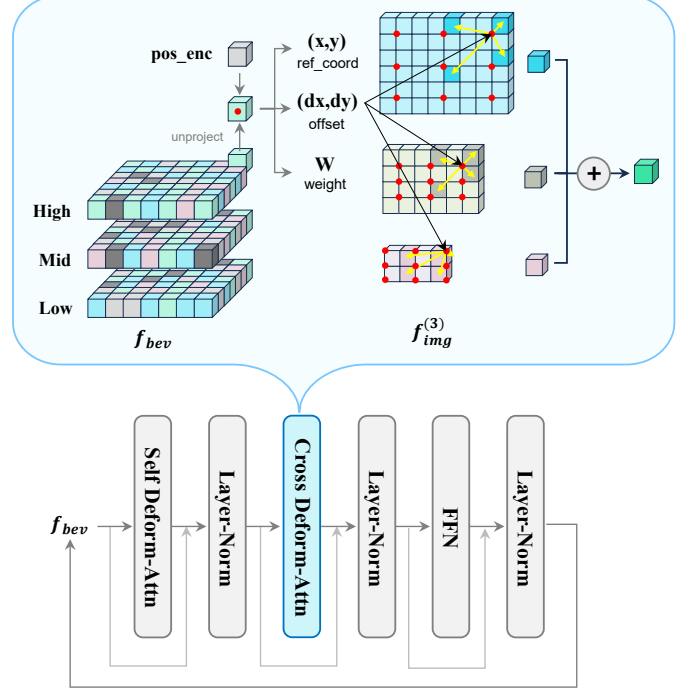


Fig. 5. Architecture of Driver/Modifier Transformer decoders. Cascaded decoders process learnable 3-layer f_{bev} , where Cross Deformable Attention enables BEV-to-multi-view semantic interaction. Modifier stages maintain independent cross-attention modules while sharing other components.

introduce high-frequency noise disrupting BEV continuity, we incorporate gating units g_{vox} for voxel features in all cascaded modules inputs (except the drive stage which must use f_{vox} to initialize queries). Simultaneously, a learnable position encoding vector $pos_{enc} \in \mathbb{R}^{Z \times X}$, shared across all-scale voxel features through interpolation sampling, is additionally incorporated. The Modifier-T shares Driver-T's architecture but introduces:

- Resolution-specific cross-attention with shared other layers balances scale adaptation and efficiency.
- Progressively increasing the number of sampling points \mathcal{P} (from 2 to 3 to 4) while maintaining a fixed 2-level depth broadens the context at higher resolutions.

E. BEV-GT Decoder and Multi-Scale Supervision

The RAF module generates multi-scale residual features $\{f'_{bevi}\}_{i=1}^4$ decoded into segmentation predictions $\{\hat{TP}_i\}$ via a shared-weight BEV-GT decoder (architecturally similar to the segmentation head), matching the GT-Encoder-Decoder's residual outputs $\{TP_i\}$. The accumulated features f_{bev_acc} , formed by aggregating all intermediate results are then decoded by the same head to yield the final prediction \hat{GT} .

BEV-GT decoder: A three-stage residual convolutional architecture processes input features (D, Z_i, X_i) , performing channel-wise fusion while preserving spatial dimensions. The processed features undergo channel compression through a final 1×1 convolution, projecting from dimension D to the target class dimension C .

Loss Supervision: We design a dual-branch multi-scale supervision mechanism to jointly optimize both residual representations and the final segmentation output:

- **Multi-scale Residual Token Map Loss:** For intermediate residual predictions \hat{TP}_s at each stage, we employ a configurable feature-level reconstruction loss that supports $L1/L2/Smooth - L1$ norms. To ensure training stability, instead of pixel-wise summation, we compute either channel-wise or spatial-wise differences:

$$\mathcal{L}_{TP_s} = \begin{cases} \frac{1}{ZX} \sum_{z,x} \|TP_i - \hat{TP}_i\|_p & \text{(Spatial-wise)} \\ \frac{1}{BC} \sum_{b,c} \|TP_i - \hat{TP}_i\|_p & \text{(Channel-wise)} \end{cases} \quad (5)$$

- **Adaptive Segmentation Dice Loss:** The final BEV segmentation output is supervised using a class-adaptive weighted Dice loss:

$$\mathcal{L}_{seg} = \frac{1}{C} \sum_{c=1}^C w_c \left(1 - \frac{2 \sum p_c \cdot g_c + \epsilon}{\sum p_c + \sum g_c + \epsilon} \right) \quad (6)$$

where $p_c = \sigma(\hat{y}_c)$ is the sigmoid-normalized prediction logits probability for class c , g_c denotes the original binary value of GT , and $w_c = \frac{1-f_c}{C \sum (1-f_c)}$ is the adaptive weight for class c , with f_c being class frequency. The smoothing term $\epsilon = 10^{-5}$ ensures numerical stability.

IV. EXPERIMENTS

In this section, we will elaborate on the experimental setup, the comparison between RESAR-BEV and other single-stage segmentation BEV models, as well as the impact of key modules and hyperparameters in the RESAR-BEV model on both training and final inference performance.

A. Dataset and Evaluation Protocol

Our model is evaluated on the nuScenes [40] v1.0 full dataset, comprising 850 driving scenes (700 training/150 validation) with 34149 samples captured in Boston and Singapore. The dataset provides synchronized multi-sensor data including six 360° Cameras, LiDAR, and Radar. Following the setting in BEV-Car, we focus on cost-effective but challenging sensor configurations using only Camera and Radar, targeting seven critical BEV segmentation categories: drivable area, pedestrian crossing, walkway, stop line, road divider, lane divider, and vehicle. For comprehensive evaluation, we employ multiple metrics including mIoU (mean intersection over union) for segmentation accuracy, per-class IoU for detailed category analysis, FPS (frames per second) for inference efficiency, parameter count for model complexity, as well as range interval evaluation to assess distance-dependent performance degradation, with additional testing under adverse weather conditions to examine robustness.

B. Experimental Settings

BEV Scene Configuration: We established a 100m × 100m BEV grid centered on the front-facing camera, covering ±50m along both the driving (Z-axis) and lateral direction (X-axis) with 200 × 200 resolution (0.5m / pixel). For the vertical dimension (Y-axis), we observed that insufficient resolution amplifies geometric offsets during grid-to-camera projection. Additionally, considering the uncertainty in camera height, we adopted a prior height estimate at 1m above the ground, defining a ±5m range (10m total height) with 0.2m resolution (50 grids). Subsequent vertical dimension normalization to 1/5 scale ensured efficiency. The input images from all 6 cameras were uniformly resized and cropped to (448, 672) resolution, while temporally aligned six-frame point clouds were employed to compensate the sparse Radar data.

Model Structure: Sampling coordinates are computed only for the maximum-resolution grid, with other resolutions obtained through interpolation for efficiency. All embedding layers are standardized to 128 dimensions, while compressed voxel features are integrated with learnable $1 \times Z \times X$ positional encoding. Both Driver-T and Modifier-T employ two-stage Transformer decoders, though Modifier-T's cross-attention modules operate independently across resolutions. A weighted balance is applied between four-stage resolution losses (weights 2.0/3.0/4.0/5.0) and the segmentation loss (10.0). Both residual and radar gating use channel/resolution-independent learnable vectors. Ground grid positions are permitted to dynamically deviate within ±0.6m of initial values.

C. Benchmark Performance Comparison

Overall Metrics: Our proposed RESAR-BEV model demonstrates significant advantages across multiple metrics. As shown in Tab. I, compared to LSS [15], CVT [35], BEVFormer [2], Simple-BEV [23], CRN [25], BEVGuide [26], and our primary baseline BEVCar [11], our model achieves superior performance in drivable area and lane divider segmentation, outperforming the baselines by +2.83 and +0.20 in IoU, respectively. For the combined metric of Drivable Area and Vehicle segmentation, our model exhibits a +2.05 advantage over the strongest baseline, while maintaining a +1.55 lead in the three-category combined metric. Notably, our full model contains only 23.28% of the parameters of BEVCar while achieving 4.23× faster FPS on NVIDIA A100 GPUs, also surpassing both Simple-BEV and the temporal fusion-based BEVFormer. Ablation studies reveal that the end-to-end variant without residual supervision outperforms the Camera-only version, validating the importance of Radar depth information in challenging scenarios such as nighttime and occlusions. However, the end-to-end model still falls short of our full progressive residual auto-regressive architecture, further confirming the effectiveness of our proposed residual supervision mechanism.

Robustness Performance: Our distance-based robustness analysis evaluates vehicle segmentation performance across varying distances using a 0.5m/pixel grid centered on the ego vehicle. In Tab. II, the CRN model demonstrates superior close-

TABLE I
PERFORMANCE COMPARISON ON NUSCENES DATASET

Method	Modalities	Resolution	Backbone	Segmentation (IoU%) \uparrow			mIoU% \uparrow	Parameter	FPS \uparrow
				Drivable Area	Vehicle	Lane Divider			
Camera-Only Methods									
LSS [15] [†]	C	128×352	EfficientNet-B0	72.94	32.07	19.96	52.51 / 41.66	14.3M	25.0
CVT [35]	C	224×448	EfficientNet-B4	52.66	24.30	—	38.48 / —	4.3M	34.0
BEVFormer [2] [†]	C	900×1600	ResNet-101	77.50	46.70	23.90	62.10 / 49.37	75.0M	1.7
BEVFormer-S [2] [†]	C	900×1600	ResNet-101	80.70	43.20	21.30	61.95 / 48.40	68.7M	—
Camera+Radar Methods									
Simple-BEV [23]	C+R	448×800	ResNet-101	—	53.17	—	— / —	42.2M	7.6
CRN [25]	C+R	224×480	R50	80.42	55.30	—	67.86 / —	76.0M	25.0
BEVGuide [26] [†]	C+R	224×480	EfficientNet	76.70	59.20	44.20	67.95 / 60.03	—	24.0
BEVCar [11]	C+R	448×672	ViT-B/14	80.60	55.70	43.90	68.15 / 60.06	137.0M	2.6
Our Approach									
RESAR-Camera	C	448×672	ResNet-101	76.88	46.60	40.20	61.74 / 54.56	30.8M	17.1
RESAR-E2E	C+R	448×672	ResNet-101	77.10	52.90	41.50	65.00 / 57.17	31.0M	15.5
RESAR-Standard	C+R	448×672	ResNet-101	83.53	56.87	44.43	70.20 / 61.61	31.9M	14.6

Abbr. : C: Camera, R: Radar; [†]: Results reproduced from official implementations; **Bold**: Best performance in each category; \uparrow/\downarrow : higher/lower are better.

We evaluate RESAR-BEV against Camera-only and Camera-Radar unidirectional end-to-end baseline models on the nuScenes validation set. To account for variations across different approaches, we evaluate three key autonomous driving segmentation tasks: Drivable Area, Vehicle, and Lane Divider using both individual IoU and mIoU (left: first two categories' average; right: all three). We Also compare model parameters and inference speed (FPS on Nvidia A100 GPU) for assessing real-time performance in autonomous driving systems. Ablation studies validate RESAR's camera-only and end-to-end configurations.

range (0 – 20m) detection by effectively combining Camera and Radar modalities with its dedicated vehicle segmentation head. While our model achieves comparable performance to BEV-Car in mid-range (20 – 35m) scenarios, it significantly outperforms all baselines by 40.8% for long-range (35 – 50m) detection. The overall performance improvement of 1.2% across all ranges (0 – 50m) can be attributed to our progressive residual refinement strategy, which first captures coarse vehicle locations before performing fine-grained residual corrections, combined with the robust depth estimation provided by Radar fusion, particularly beneficial in challenging conditions like low-light environments or occluded scenarios.

cal driving scenarios: sunny (optimal), rainy (moderate), and dark (severe). In Tab. III, our key findings: (1) All models demonstrate improved drivable area and vehicle segmentation performance in rainy conditions, attributed to reduced vehicular occlusion and more comprehensive Camera coverage compensating for Radar deficiencies, while lane segmentation accuracy declines due to water surface reflections. (2) Night degrades all models as cameras lose reliable visual cues while Radar remains sparse. The comprehensive retesting confirms our full model's robustness (54.0% mIoU), achieving a 2.48% advantage over BEVCar (51.52%) across all categories and conditions.

TABLE II
PERCEPTION RANGE PERFORMANCE COMPARISON

Method	Modality	0-50m	Range Intervals (m)		
			0-20m	20-35m	35-50m
CVT	C	24.3	37.4	25.0	10.5
Simple-BEV	C+R	53.2	71.9	52.8	34.8
CRN	C+R	55.3	82.1	47.6	36.1
BEVCar	C+R	55.7	75.3	52.2	39.6
RESAR	C	46.6	69.2	44.9	25.5
RESAR-E2E	C+R	52.9	74.0	47.8	36.8
RESAR	C+R	56.9	77.6	52.2	40.8

Abbr.: C: Camera; R: Radar; All values represent mIoU (%).

Our environment-based robustness analysis reveals complementary Camera-Radar limitations. Using the validation split from [11], we benchmarked our full progressive refinement model, its end-to-end variant, and BEVCar across three criti-

D. Ablation Study

Through comparative analysis of the complete model, Camera-only model, and end-to-end model without progressive supervision during training (Fig. 6), we observe distinct behavioral patterns: The end-to-end model demonstrates the fastest convergence rate (63.5% training accuracy improvement) due to its single segmentation loss objective, yet achieves only 49.6% validation mIoU, indicating severe overfitting from simplistic end-to-end mapping. In contrast, our complete model with residual auto-regressive supervision exhibits slower convergence but significantly reduced train-validation performance gap, ultimately attaining 54.0% validation mIoU - a benefit attributable to the implicit regularization provided by multi-stage supervision. The Camera-only model performs poorest (44.2% mIoU), reaffirming the critical role of Radar depth information in BEV perception.

TABLE III
PERFORMANCE COMPARISON UNDER
DIFFERENT WEATHER CONDITIONS

Method	Categories						
	D.A.	P.C.	W.W.	S.L.	R.L.	L.D.	V.H.
Sunny Conditions							
BEVCar	82.3	51.9	62.5	41.7	44.2	46.2	55.8
Us-E2E	78.4	47.3	61.2	41.0	44.5	42.1	53.2
RESAR	84.5	50.7	65.3	43.2	48.5	45.9	57.9
Rainy Conditions							
BEVCar	82.6	48.5	58.0	35.4	41.8	45.3	56.9
Us-E2E	79.6	44.7	58.6	37.8	39.9	41.5	55.3
RESAR	86.9	47.5	62.5	40.8	46.7	44.1	59.5
Night Conditions							
BEVCar	76.9	40.2	50.1	31.5	35.7	40.2	54.3
Us-E2E	73.2	40.0	48.2	32.1	33.0	40.3	49.5
RESAR	79.2	42.5	53.8	38.2	40.5	42.8	53.1

Abbr. : D.A.: Drivable Area, P.C.: Pedestrian Crossing, W.W.: Walkway, S.L.: Stop Line, R.L.: Road Divider, L.D.: Lane Divider, V.H.: Vehicle; All values represent mIoU (%).

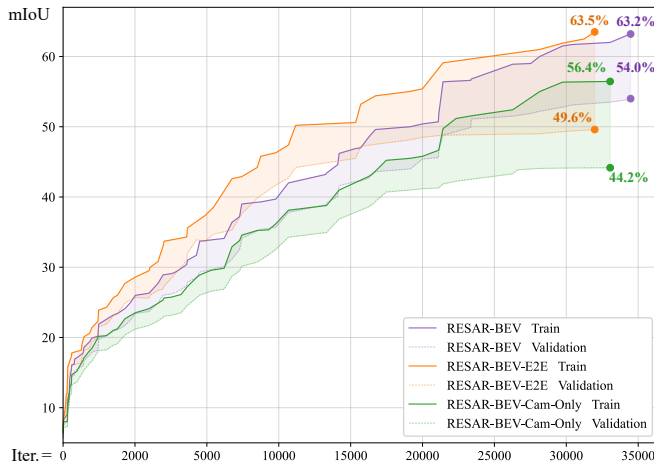


Fig. 6. Training and validation mIoU trajectories for complete RESAR-BEV model versus two ablated models across iterations (32 batches/iteration). The semi-transparent bands indicate performance gaps between training and validation sets.

We conducted comprehensive ablation studies on our RESAR-BEV, evaluating both key modules and critical parameters while comparing inference speed (FPS), model size (parameters), and mean accuracy (mIoU), as detailed in Tab. IV.

Module Ablation: (1) The Camera-only variant eliminates Radar feature extraction but introduces learnable initialization queries $Q_{init} \in \mathcal{R}^{(C, Z/8, X/8)}$ as substitutes, resulting in comparable parameter counts (-3.4%) with 2.5% faster inference yet 9.8% mIoU degradation. (2) Replacing residual learning with direct downsampling causes significant 6.2% accuracy drop. (3) Removing progressive supervision leads to 4.4% performance reduction. (4) Eliminating attention pooling in our proposed VEF decreases accuracy by 5.7% .

Parameter Ablation: (1) Disabling both residual gating (for

token maps alignment) and voxel gating (for Radar feature modulation) reduces mIoU by 4.7% . (2) Fixing three-layer BEV grid offsets decreases accuracy by 5.2% . (3) Expanding cascade depth from 2 to 4 levels increases parameters by 3.8% and inference time by 32% , yielding marginal 0.4% accuracy gain - our attention visualization reveals sparse activation patterns in deeper layers, suggesting limited utility. Our full model achieves optimal balance with 54.0% mIoU and real-time 14.6 FPS performance.

TABLE IV
MODULE & HYPERPARAMETER ABLATION STUDIES

Category	Variant	Categories		
		FPS	Param.	mIoU
Module Ablations				
1	Camera Only	17.1	30.8M	44.2
2	Pyramid or Residual	15.1	31.9M	47.8
3	End to End	15.5	31.0M	49.6
4	VFE Attention	15.2	31.8M	51.0
Hyperparameter Ablations				
5	Voxel, Residual-gate	14.9	31.9M	49.3
6	Learnable Height Offset	14.8	31.9M	48.8
7	4 Driver-Modifier Layers	9.9	33.1M	54.4
8	Full Model	14.6	31.9M	54.0

Abbr. : FPS: Frames Per Second, Param.: Parameters (in millions), mIoU: mean Intersection over Union (%).

E. Visualization

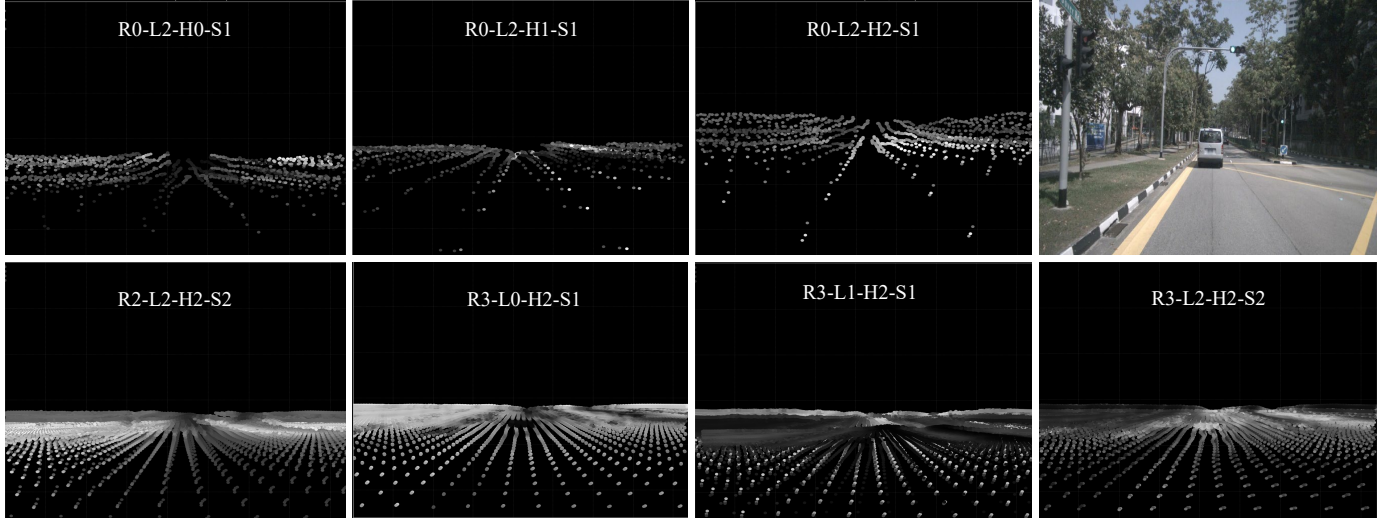
We first visualize the progressive residual prediction process and final threshold-filtered results across sunny, rainy, and night scenarios (Fig. 7). Each step represents the accumulated upsampling of all previously generated \hat{TPs} . Key observations: (1) The first two iterations demonstrate clear progression from low-resolution blurring to higher-resolution segmentation, with visual quality improving as predicted by our supervision strategy; (2) The fourth iteration shows only marginal refinement over the third, primarily in fine edge details; (3) For nighttime scenarios, the model exhibits reduced environmental perception capability, resulting in extensive low-confidence background regions, whereas sunny/rainy conditions show significantly fewer such artifacts. Notably, the model’s attention mechanism automatically focuses on foreground areas while suppressing uncertain background noise.

We further visualize cross-modal attention in Driver-T and Modifier-T modules, projecting into image view frustum space to correlate with road surfaces (Fig. 8). Observations show: (1) Different attention heads within the same module spontaneously attend to distinct vertical spatial information—Head0 focuses on lower regions with sampling points offset horizontally, while Head2 prioritizes higher regions with vertical sampling offsets; (2) In residual modules with lower resolution, the attention exhibits more pronounced offsets due to the smaller BEV feature plane, enabling global topological awareness, whereas higher-resolution residual modules with smaller sampling offsets focus more on local details; (3) In

	Camera Input	Radar Input	Ground Truth	Token Maps	Segment Result
Sun					
Rain					
Night					

■ Drivable_area
 ■ Ped_crossing
 ■ Walkway
 ■ Stop_line
 ■ Road_divider
 ■ Lane_divider
 ■ Vehicles

Fig. 7. Progressive Multi-modal BEV Semantic Segmentation via Residual Auto-regression Across Diverse Environmental Conditions. The model integrates synchronized inputs from six surround-view cameras and six consecutive frames of radar point clouds through four-step residual auto-regression (shown as accumulated residuals), outputting seven-class BEV segmentation.



Abbr. : R: Residual stage; L: Image feature level; H: Attention head; S: Driver-T/Modifier-T Decoder layer.

Fig. 8. The visualization of cross-modal attention weights in Driver-T and Modifier-T under the image view, demonstrating a distinct vertical and road-category hierarchical attention pattern across different residual modules, image feature layers, attention heads, and decoder module levels.

deeper residual modules, the decoder’s different hierarchical levels and attended image feature layers reveal divergent focus patterns—the model may concentrate on non-vehicle road surfaces, vehicle regions, or pedestrian walkways across different layers. While the underlying regularity remains elusive, it is evident that the model captures distinct segmentation categories through varied attention processes.

This multi-stage evolution aligns perfectly with our residual learning objectives, where early stages establish structural context while later stages focus on local detail recovery.

V. CONCLUSION

Our RESAR-BEV framework introduces progressive residual autoregressive learning for BEV segmentation, addressing cross-modal misalignment, error accumulation, and interpretability limitations of single-step approaches. By decomposing the task into multi-stage residual optimization with hierarchical supervision, our method boosts accuracy while maintaining real-time speed. A geometry-guided radar-aided feature querying mechanism and adaptive height offset strategy ensure robustness in long-range and low-light scenarios,

validated on nuScenes. Our human cognition-inspired learning enables interpretable refinement, while a cost-efficient camera-radar fusion and two-stage training enhance generalization. Ablations verify critical components like multi-scale losses and autoregressive optimization. Future work will explore the temporal-residual architectures with dynamic resolution.

REFERENCES

- [1] Y. Kim and D. Kum, “Deep learning based vehicle position and orientation estimation via inverse perspective mapping image,” in *2019 IEEE Intelligent Vehicles Symposium (IV)*, 2019, pp. 317–323.
- [2] Z. Li, W. Wang, H. Li, E. Xie, C. Sima, T. Lu, Q. Yu, and J. Dai, “Bevformer: Learning bird’s-eye-view representation from lidar-camera via spatiotemporal transformers,” *IEEE Transactions on Pattern Analysis and Machine Intelligence*, vol. 47, no. 3, pp. 2020–2036, 2025.
- [3] Z. Zhang, M. Xu, W. Zhou, T. Peng, L. Li, and S. Poslad, “Bev-locator: An end-to-end visual semantic localization network using multi-view images,” *Science China Information Sciences*, vol. 68, no. 2, p. 122106, 2025.
- [4] S. Chen, X. Wang, T. Cheng, Q. Zhang, C. Huang, and W. Liu, “Polar parametrization for vision-based surround-view 3d detection,” *arXiv preprint arXiv:2206.10965*, 2022.
- [5] Y. Jiang, L. Zhang, Z. Miao, X. Zhu, J. Gao, W. Hu, and Y.-G. Jiang, “Polarformer: Multi-camera 3d object detection with polar transformer,” in *Proceedings of the AAAI conference on Artificial Intelligence*, vol. 37, no. 1, 2023, pp. 1042–1050.
- [6] J. Huang and G. Huang, “Bevdet4d: Exploit temporal cues in multi-camera 3d object detection,” *arXiv preprint arXiv:2203.17054*, 2022.
- [7] Y. Zhang, Z. Zhu, W. Zheng, J. Huang, G. Huang, J. Zhou, and J. Lu, “Beverse: Unified perception and prediction in birds-eye-view for vision-centric autonomous driving,” *arXiv preprint arXiv:2205.09743*, 2022.
- [8] J. Pan, X. Huang, S. Luo, and F. Ma, “Bev transformer for visual 3d object detection applied with retentive mechanism,” *Transactions of the Institute of Measurement and Control*, p. 01423312241308367, 2025.
- [9] J. Zhang, Y. Zhang, Y. Qi, Z. Fu, Q. Liu, and Y. Wang, “Geobev: Learning geometric bev representation for multi-view 3d object detection,” in *Proceedings of the AAAI Conference on Artificial Intelligence*, vol. 39, no. 9, 2025, pp. 9960–9968.
- [10] D. A. Oladele, E. D. Markus, and A. M. Abu-Mahfouz, “Bev-cam3d: A unified bird’s-eye view architecture for autonomous driving with monocular cameras and 3d point clouds,” *AI*, vol. 6, no. 4, 2025.
- [11] J. Schramm, N. Vödisch, K. Petek, B. R. Kiran, S. Yogamani, W. Burghard, and A. Valada, “Bevcar: Camera-radar fusion for bev map and object segmentation,” in *2024 IEEE/RSJ International Conference on Intelligent Robots and Systems (IROS)*, 2024, pp. 1435–1442.
- [12] W. Jun and S. Lee, “A comparative study and optimization of camera-based bev segmentation for real-time autonomous driving,” *Sensors*, vol. 25, no. 7, p. 2300, 2025.
- [13] C. Lu, M. J. G. van de Molengraft, and G. Dubbelman, “Monocular semantic occupancy grid mapping with convolutional variational encoder–decoder networks,” *IEEE Robotics and Automation Letters*, vol. 4, no. 2, pp. 445–452, 2019.
- [14] B. Pan, J. Sun, H. Y. T. Leung, A. Andonian, and B. Zhou, “Cross-view semantic segmentation for sensing surroundings,” *IEEE Robotics and Automation Letters*, vol. 5, no. 3, pp. 4867–4873, 2020.
- [15] J. Philion and S. Fidler, “Lift, splat, shoot: Encoding images from arbitrary camera rigs by implicitly unprojecting to 3D,” in *European Conference on Computer Vision*, 2020, pp. 194–210.
- [16] J. Huang, G. Huang, Z. Zhu, Y. Ye, and D. Du, “BEVDet: High-performance multi-camera 3D object detection in bird-eye-view,” *arXiv preprint arXiv:2212.11790*, 2021.
- [17] A. Hu, Z. Murez, N. Mohan, S. Dudas, J. Hawke, V. Badrinarayanan, R. Cipolla, and A. Kendall, “Fiery: Future instance prediction in bird’s-eye view from surround monocular cameras,” in *2021 IEEE/CVF International Conference on Computer Vision (ICCV)*, 2021, pp. 15253–15262.
- [18] Y. Wang, V. C. Guizilini, T. Zhang, Y. Wang, H. Zhao, and J. Solomon, “Det3d: 3d object detection from multi-view images via 3d-to-2d queries,” in *Conference on Robot Learning*. PMLR, 2022, pp. 180–191.
- [19] X. Zhu, W. Su, L. Lu, B. Li, X. Wang, and J. Dai, “Deformable detr: Deformable transformers for end-to-end object detection,” in *International Conference on Learning Representations*, 2020.
- [20] L. Peng, Z. Chen, Z. Fu, P. Liang, and E. Cheng, “Bevsegformer: Bird’s eye view semantic segmentation from arbitrary camera rigs,” in *Proceedings of the IEEE/CVF Winter Conference on Applications of Computer Vision*, 2023, pp. 5935–5943.
- [21] Z. Liu, H. Tang, A. Amini, X. Yang, H. Mao, D. L. Rus, and S. Han, “Bevfusion: Multi-task multi-sensor fusion with unified bird’s-eye view representation,” in *2023 IEEE international conference on robotics and automation (ICRA)*. IEEE, 2023, pp. 2774–2781.
- [22] X. Bai, Z. Hu, X. Zhu, Q. Huang, Y. Chen, H. Fu, and C.-L. Tai, “TransFusion: Robust LiDAR-camera fusion for 3D object detection with transformers,” in *IEEE/CVF Conference on Computer Vision and Pattern Recognition*, 2022, pp. 1080–1089.
- [23] A. W. Harley, Z. Fang, J. Li, R. Ambrus, and K. Fragiadaki, “Simple-BEV: What really matters for multi-sensor BEV perception?” in *IEEE International Conference on Robotics and Automation*, 2023, pp. 2759–2765.
- [24] N. Hendy, C. Sloan, F. Tian, P. Duan, N. Charchut, Y. Xie, C. Wang, and J. Philbin, “FISHING Net: Future inference of semantic heatmaps in grids,” *arXiv preprint arXiv:2006.09917*, 2020.
- [25] Y. Kim, J. Shin, S. Kim, I.-J. Lee, J. W. Choi, and D. Kum, “CRN: Camera radar net for accurate, robust, efficient 3D perception,” in *International Conference on Computer Vision*, 2023, pp. 17569–17580.
- [26] Y. Man, L.-Y. Gui, and Y.-X. Wang, “BEV-guided multi-modality fusion for driving perception,” in *IEEE/CVF Conference on Computer Vision and Pattern Recognition*, 2023, pp. 21960–21969.
- [27] C. Yang, Y. Chen, H. Tian, C. Tao, X. Zhu, Z. Zhang, G. Huang, H. Li, Y. Qiao, L. Lu *et al.*, “Bevformer v2: Adapting modern image backbones to bird’s-eye-view recognition via perspective supervision,” in *Proceedings of the IEEE/CVF Conference on Computer Vision and Pattern Recognition*, 2023, pp. 17830–17839.
- [28] S. Wang, Y. Liu, T. Wang, Y. Li, and X. Zhang, “Exploring object-centric temporal modeling for efficient multi-view 3d object detection,” in *Proceedings of the IEEE/CVF international conference on computer vision*, 2023, pp. 3621–3631.
- [29] M. Chang, X. Zhang, R. Zhang, Z. Zhao, G. He, and S. Liu, “Recurrentbev: A long-term temporal fusion framework for multi-view 3d detection,” in *European Conference on Computer Vision*. Springer, 2024, pp. 131–147.
- [30] P. Li, W. Shen, Q. Huang, and D. Cui, “Dualbev: Unifying dual view transformation with probabilistic correspondences,” in *European Conference on Computer Vision*. Springer, 2024, pp. 286–302.
- [31] T. Tang, D. Wei, Z. Jia, T. Gao, C. Cai, C. Hou, P. Jia, K. Zhan, H. Sun, F. JingChen *et al.*, “Bev-ts: Text-scene retrieval in bev space for autonomous driving,” in *Proceedings of the AAAI Conference on Artificial Intelligence*, vol. 39, no. 7, 2025, pp. 7275–7283.
- [32] R. A. Khan, Y. Luo, and F.-X. Wu, “Rms-unet: Residual multi-scale unet for liver and lesion segmentation,” *Artificial Intelligence in Medicine*, vol. 124, p. 102231, 2022.
- [33] K. Tian, Y. Jiang, Z. Yuan, B. Peng, and L. Wang, “Visual autoregressive modeling: Scalable image generation via next-scale prediction,” *Advances in neural information processing systems*, vol. 37, pp. 84839–84865, 2024.
- [34] D. Lee, C. Kim, S. Kim, M. Cho, and W.-S. Han, “Autoregressive image generation using residual quantization,” in *Proceedings of the IEEE/CVF Conference on Computer Vision and Pattern Recognition*, 2022, pp. 11523–11532.
- [35] B. Zhou and P. Krähenbühl, “Cross-view transformers for real-time map-view semantic segmentation,” in *IEEE/CVF Conference on Computer Vision and Pattern Recognition*, 2022, pp. 13750–13759.
- [36] Z. Yu, W. Wan, M. Ren, X. Zheng, and Z. Fang, “SparseFusion3D: Sparse sensor fusion for 3D object detection by radar and camera in environmental perception,” *IEEE Intelligent Vehicles Symposium*, 2023.
- [37] K. He, X. Zhang, S. Ren, and J. Sun, “Deep residual learning for image recognition,” in *Proceedings of the IEEE conference on computer vision and pattern recognition*, 2016, pp. 770–778.
- [38] Y. Zhou and O. Tuzel, “Voxelnet: End-to-end learning for point cloud based 3d object detection,” in *Proceedings of the IEEE conference on computer vision and pattern recognition*, 2018, pp. 4490–4499.
- [39] Z. Xia, X. Pan, S. Song, L. E. Li, and G. Huang, “Vision transformer with deformable attention,” in *Proceedings of the IEEE/CVF conference on computer vision and pattern recognition*, 2022, pp. 4794–4803.
- [40] H. Caesar, V. Bankiti, A. H. Lang, S. Vora, V. E. Liong, Q. Xu, A. Krishnan, Y. Pan, G. Baldan, and O. Beijbom, “nuScenes: A multimodal dataset for autonomous driving,” in *IEEE/CVF Conference on Computer Vision and Pattern Recognition*, 2020, pp. 11618–11628.